Journal of Environmental Management 268 (2020) 110650

Contents lists available at ScienceDirect

Journal of Environmental Management

journal homepage: http://www.elsevier.com/locate/jenvman

Research article

Real-time source contribution analysis of ambient ozone using an enhanced meta-modeling approach over the Pearl River Delta Region of China

Tingting Fang [a], Yun Zhu [a,b,*], Jicheng Jang [a], Shuxiao Wang [c], Jia Xing [c], Pen-Chi Chiang [d,e], Shaojia Fan [b], Zhiqiang You [a], Jinying Li [a]

[a] Guangdong Provincial Key Laboratory of Atmospheric Environment and Pollution Control, College of Environment and Energy, South China University of Technology, Guangzhou Higher Education Mega Center, Guangzhou, 510006, China
[b] Southern Marine Science and Engineering Guangdong Laboratory, Sun Yat-Sen University, Zhuhai, 519000, China
[c] State Key Joint Laboratory of Environment Simulation and Pollution Control, School of Environment, Tsinghua University, Beijing, 100084, China
[d] Graduate Institute of Environmental Engineering, National Taiwan University, Taipei, 10673, Taiwan
[e] Carbon Cycle Research Center, National Taiwan University, 10672, Taiwan

ARTICLE INFO

Keywords:
O_3
Nonlinear response
O_3-NO_x-VOC relationships
Source contribution
Response surface modeling

ABSTRACT

The nonlinear response of O_3 to nitrogen oxides (NO_x) and volatile organic compounds (VOC) is not conducive to accurately identify the various source contributions and O_3-NO_x-VOC relationships. An enhanced meta-modeling approach, polynomial functions based response surface modeling coupled with the sectoral linear fitting technique (pf-ERSM-SL), integrating a new differential method (DM), was proposed to break through the limitation. The pf-ERSM-SL with DM was applied for analysis of O_3 formation regime and real-time source contributions in July and October 2015 over the Pearl River Delta Region (PRD) of Mainland China. According to evaluations, the pf-ERSM-SL with DM was proven to be effective in source apportionment when the traditional sensitivity analysis was unsuitable for deriving the source contributions in the nonlinear system. After diagnosing the O_3-NO_x-VOC relationships, O_3 formation in most regions of the PRD was identified as a distinctive NO_x-limited regime in July; in October, the initial VOC-limited regime was found at small emission reductions (less than 22–44%), but it will transit to NO_x-limited when further reductions were implemented. Investigation of the source contributions suggested that NO_x emissions were the dominated contributor when turning-off the anthropogenic emissions, occupying 85.41–94.90% and 52.60–75.37% of the peak O_3 responses in July and October respectively in the receptor regions of the PRD; NO_x emissions from the on-road mobile source (NO_x_ORM) in Guangzhou (GZ), Dongguan&Shenzhen (DG&SZ) and Zhongshan (ZS) were identified as the main contributors. Consequently, the reinforced control of NO_x_ORM is highly recommended to lower the ambient O_3 in the PRD effectively.

1. Introduction

As a kind of air pollutant, tropospheric ozone (O_3) significantly influences the human health and global climate (Shindell et al., 2012; Turner et al., 2016). Following the rapid urbanization and industrialization, tropospheric ozone pollution becomes more evident, while the levels of fine particulate matters ($PM_{2.5}$) have been effectively alleviated in China (Li et al., 2019; Lu et al., 2018; Strode et al., 2019). The Pearl River Delta Region (PRD), one of the three major city clusters in China, has especially experienced great O_3 episodes in the past few years (Li et al., 2019; Shen et al., 2019; Wang et al., 2019). As a kind of secondary pollutant forming in the troposphere while nitrogen oxides (NO_x) reacts with volatile organic compounds (VOC) in the sunshine, O_3 has a complex formation mechanism, which is demonstrated by its nonlinear response to NO_x and VOC emission changes under different chemical regimes (Chatani et al., 2014; Jin et al., 2017; Ou et al., 2016; Tan et al., 2018; Wang et al., 2017b; Zou et al., 2019). Above all, O_3 concentrations are contributed by diverse anthropogenic emission sectors of NO_x and VOC in local and regional scales simultaneously (Han et al., 2018; Li et al., 2012; Wang et al., 2016; Yang et al., 2019; Zhang et al., 2016). Moreover, source contribution results vary with time and space; therefore, it is of particular importance to determine the O_3-NO_x-VOC

* Corresponding author. Guangdong Provincial Key Laboratory of Atmospheric Environment and Pollution Control, College of Environment and Energy, South China University of Technology, Guangzhou Higher Education Mega Center, Guangzhou, 510006, China.
E-mail address: zhuyun@scut.edu.cn (Y. Zhu).

https://doi.org/10.1016/j.jenvman.2020.110650
Received 7 February 2020; Received in revised form 1 April 2020; Accepted 23 April 2020
Available online 14 May 2020

relationships and key emission source contribution to O_3 for designing a scientific O_3 control policy, especially in the PRD region which is dominated by O_3 pollution (Li et al., 2014; Wang et al., 2017a, 2019).

Brute-force method (BFM) is the simplest approach to analyze the O_3 sensitivity to precursor emission changes, which apportions the sensitivity coefficients by subtracting a detached scenario with a disturbed control factor from a base scenario (Burr and Zhang, 2011; Lin et al., 2005; Odman et al., 2009; Sharma et al., 2016). As a more advanced method, decoupled direct method (DDM) directly calculates the first-order sensitivity coefficients of the pollutant response to changes in model input parameters using mathematical technology (Dunker, 1984; Dunker et al., 2002; Luecken et al., 2018). Nevertheless, the impacts of emission control calculated by the BFM or DDM on O_3 concentration can be viewed as the source contributions only in the linear system (Clappier et al., 2017). An extended high-order DDM (HDDM) was developed sequentially to make characterization of the nonlinear responses (Choi et al., 2014; Collet et al., 2017; Hakami et al., 2004; Itahashi et al., 2013; Wang et al., 2011b). However, the HDDM can hardly predict the O_3 response when there are multiple (>3) variables and large perturbations (Dunker et al., 2002; Itahashi et al., 2015). In my best knowledge, as a technique allocating the O_3 response to different sources using tagged tracers, ozone source apportionment technology (OSAT) ensures that the sum of individual contributions is equal to the actual O_3 response, and also enhances the calculation efficiency for multiple variables (Li et al., 2012, 2016; Moghani et al., 2018; Sharma et al., 2017). Whereas the main limitation of OSAT is that it cannot capture the O_3 destruction mechanism caused by the NO titration, resulting in the overestimated contribution from a particular source (Dunker et al., 2002; Itahashi et al., 2015). More importantly, methods above based on the air quality model are both unable to assess the O_3 response to dynamic emission changes in real-time, which largely limits their application in designing effective O_3 control policies (Xing et al., 2018; Zhao et al., 2015). Thereby, a series of meta-models of air quality modeling, including response surface modeling (RSM), extended RSM (ERSM), and polynomial functions based RSM (pf-RSM), were developed by our international research team; they can rapidly estimate the O_3 response under various control scenarios and build the nonlinear system of O_3-NO_x-VOC (Wang et al., 2011a; Xing et al., 2011, 2017, 2018; Zhao et al., 2015, 2017). Sensitivity obtained by the BFM was utilized in traditional RSM to derive the source contributions, which can provide the impact information resulted from a specific emission control but is inapplicable for source apportionment of secondary pollutant (Clappier et al., 2017; Cohan et al., 2005).

Accordingly, an enhanced meta-modeling approach, polynomial functions based ERSM coupled with the sectoral linear fitting technique (pf-ERSM-SL), integrating a new differential method (DM), was developed in our study. As an extended pf-RSM technique using polynomial functions, the pf-ERSM has the identical structure with the ERSM; the SL provides an efficient way to estimate the emission weight of each sector to allocate the multisectoral contributions; while the DM can divide the emission perturbations into countless tiny intervals and sum the correspondingly tiny O_3 response in each interval, consequently quantifying the nonlinear source contributions. The O_3-NO_x-VOC relationships and dynamic source contributions from multiple regions and sectors to O_3 in the case study of the PRD are identified by the pf-ERSM-SL with DM, and the suggestions for O_3 control policies are provided.

2. Methodology

The analysis process of O_3 formation regime and source contributions by the pf-ERSM-SL with DM is given in Fig. 1. First, the configuration of modeling domain in Weather Research and Forecast Model (WRF) and Community Multi-scale Air Quality Model for Communities (CMAQ), and the experimental design of control matrix based on the selected control factors were determined; then, the meteorological conditions were simulated by the WRF model, which was then utilized to drive the CMAQ simulations over the PRD region. Second, the pf-ERSM-SL system was built upon the WRF-CMAQ simulations; the Out-of-sample (OOS) validation was used to examine the performance of pf-ERSM-SL, and the applicability of DM in source apportionment was also evaluated. Finally, the pf-ERSM-SL with DM was applied to diagnose the O_3-NO_x-VOC relationships and further apportion the contribution of NO_x and VOC emissions from different regions and sectors to O_3 response.

2.1. WRF-CMAQ modeling domain and configuration

In the WRF-CMAQ modeling system, three nested modeling domains with 27 km, 9 km and 3 km horizontal resolutions were used (Fig. 2a). Covering the whole Pearl River Dealt Region, the innermost 3-km domain was divided into 7 regions, including Shunde (SD), Foshan (FS), Guangzhou (GZ), Zhongshan (ZS), Jiangmen (JM), Dongguan and Shenzhen (DG&SZ) and all the other regions in the D3 domain (OTH) (Fig. 2b). The national-controlled air-monitoring sites in the 6 receptor

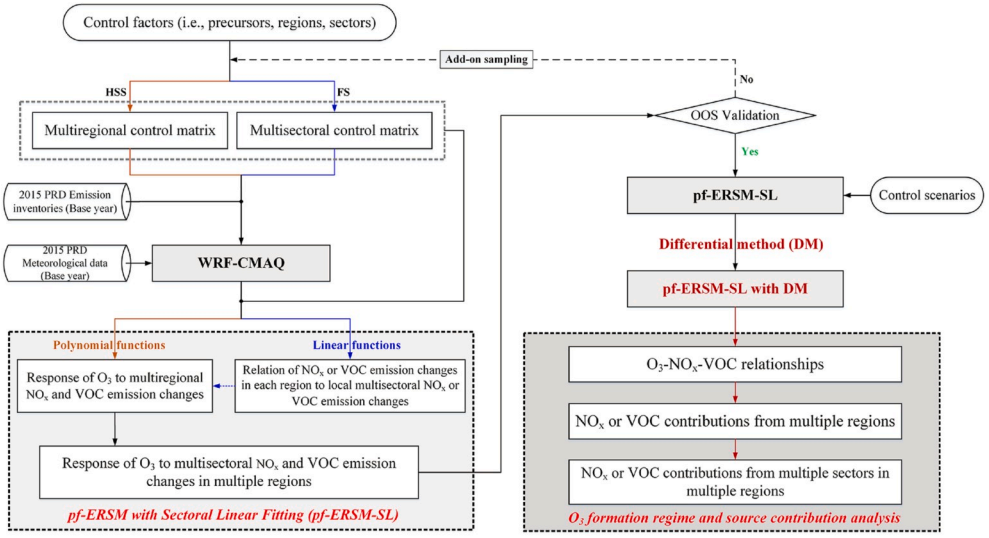

Fig. 1. The flow scheme for analysis of O_3 formation regime and source contributions by the pf-ERSM-SL with DM. HSS - Hamersley quasi-random Sequence Sampling; FS - Fixed Value Sampling; OOS - Out-of-sample.

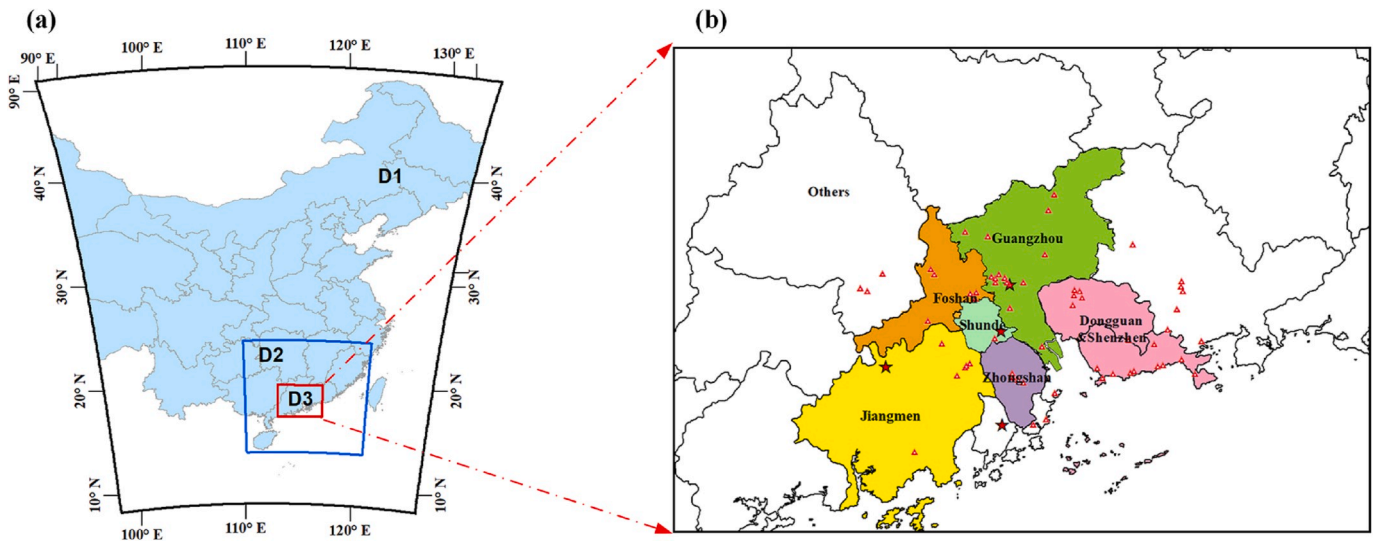

Fig. 2. Defined (a) WRF-CMAQ simulation domain and (b) regions and national-controlled air-monitoring sites in the D3 domain. The triangular points represent the monitor sites in the PRD; the pentacle points represent the selected monitor sites for evaluation of the model performance.

regions (except the OTH) were chosen to represent the air quality of these regions. Meteorological simulations with the WRF in version 3.9.1 (http://www2.mmm.ucar.edu/wrf/) and air quality simulations with the CMAQ in version 5.2 (http://www.epa.gov/cmaq) both used one-way nesting. In the outer 27-km domain, the initial and boundary conditions of the CMAQ simulations were on the basis of the default configuration in the CMAQ model. Simulations in the outer and middle domains generated boundary conditions for 9-km in the middle and 3-km inside respectively. Tsinghua University provided the emission inventories of the outer and middle domains, and the research group from Tsinghua University and South China University of Technology developed the 2015 emission inventory of the inner 3-km domain cooperatively. The details of the anthropogenic emission inventory for the precursors of O_3 in the D3 domain are given in Table S1. In the PRD, the peak O_3 concentrations usually occur in the summer, while the fall experiences the highest monthly mean O_3 concentration (Liu et al., 2010; Zheng et al., 2010). Therefore, July and October in 2015 were selected for simulations of O_3 and its precursors to represent these two seasons, and a 7 days spin-up time was used for the simulations of July and October to exclude the effect of initial condition. The hourly concentrations of O_3 and its precursors at each grid under experimental designed scenarios were simulated by the CMAQ; then the monthly averages of daily 1 h maxima O_3 and 24 h averaged NO_x and VOC, which were calculated from the hourly simulated results, were combined with the corresponding emission ratio to input into the pf-ERSM-SL for building the nonlinear system of O_3-NO_x-VOC.

Normalized Mean Bias (NMB) and Correlation coefficient (R) were chosen as indexes of model prediction performance (Text S1). By comparing the mean of hourly predicted and measured values at central monitoring sites of the D3 domain (Table S2), the performance of the WRF model was assessed. In terms of wind speed, the R value is more than 0.5 at both of the two sites, but the predicted wind speed is relatively deviated high (NMB is 127.81% in July and 76.95% in October) in Sugang; the R value is larger than 0.7 for relative humidity and temperature. The CMAQ model performance was evaluated by comparing the simulated and observed results at four representative sites in GZ, SD, JM, and OTH in the air quality monitoring networks of the PRD, representing the urban site (GD Business College), industrial site (Sugang), rural site (Shuangqiao) and coastal site (Doumen), respectively (Fig. S1). The NMB for O_3 ranges from −12.22% to 4.81% and −18.81% to 15.75% in July and October, respectively, which is mostly within the receivable performance range of ±15% proposed by Emery et al. (2017) based on the researches of photochemical modeling in the U.S. over the last decade, and also comparable to these in other published articles (Nguyen et al., 2019; Ou et al., 2016; Qin et al., 2019). Additionally, according to the criteria (>0.5) and goal (>0.75) of R for O_3 simulations recommended by Emery et al. (2017), the R value with a range from 0.72 to 0.78 in our study also proven to be desirable. Taken together, the magnitude and diurnal variation, and the seasonal trend of O_3 in 2015 are reasonably well predicted.

2.2. Development of the pf-ERSM-SL with differential method

2.2.1. pf-ERSM-SL

The pf-ERSM-SL using the pf-ERSM technique coupled with the SL fitting method to build the response of O_3 concentration to multiregional and multisectoral NO_x and VOC emission changes (Fig. S2). Because the pf-ERSM is identical to ERSM in structure and identical to pf-RSM in algorithm, which both had been detailed in the past researches (Long et al., 2016; Wang et al., 2011a; Xing et al., 2011, 2017, 2018; You et al., 2017; Zhao et al., 2017), therefore only the key components of the pf-ERSM are summarized in Section S1.

The development of the SL fitting method is detailed as followings. First, since NO_x and VOC are both emitted directly from the primary sources, the changes in NO_x or VOC concentration in each source region to local NO_x or VOC emission changes can be constructed by a series of linear functions expressed as equations (1) and (2). The linear relation is indicated in Fig. S3, in which the region with a high slope mostly experiences a more intensive NO_x or VOC emissions, as provided in Table S1. The high slope also means the emissions are relatively controllable, such as NO_x emissions in GZ and DG&SZ, and VOC emissions in DG&SZ.

$$\Delta Conc_{NOx_r} = a \cdot E_{NOx_r} \quad (1)$$

$$\Delta Conc_{VOC_r} = b \cdot E_{VOC_r} \quad (2)$$

where $\Delta Conc_{NOx_r}$ and $\Delta Conc_{VOC_r}$ are the changes in NO_x and VOC concentration respectively, in region r to local NO_x and VOC emission changes, and at an individual grid cell or aggregated cells in region r (r can represent any source region), the concentration can be hourly, monthly or annual means; E_{NOx_r} and E_{VOC_r} refer to the ratio of changed NO_x and VOC emissions respectively, in region r; a and b are the linear coefficients of E_{NOx_r} and E_{VOC_r}.

Second, the changes in NO_x or VOC concentration in each source region under multisectoral control scenarios were taken into the linear

Table 1
Designed scenarios in the pf-ERSM-SL.

Abbreviation	Objective	Control factor [a]	Number of cases
pf-RSM_TT	Using pf-RSM method, to create multiple regional pf-RSM in 7 regions	2 precursors including NO_x, VOC in each of the 7 regions	41 cases (Hamersley quasi-random Sequence Sampling between 0.0 and 1.5) for 7 regions together and one baseline case (=1.0)
pf-ERSM	Extended pf-RSM method, to create single regional pf-RSM in 7 regions separately	2 precursors including NO_x, VOC in each of the 7 regions	41 cases (Hamersley quasi-random Sequence Sampling between 0.0 and 1.5) for each region and one baseline case (=1.0)
SL	Sectoral linear fitting method, to create linear relation between NO_x or VOC emission changes and multisectoral NO_x or VOC emission changes in 7 regions separately	8 sectors including NO_x_ORM, NO_x _NRM, NO_x_SC, NO_x_OTH, VOC_ORM, VOC_IP, VOC_SU, VOC_OTH in each of the 7 regions	10 cases (Zeroing out one by one Sampling) for each region
OOS	Out-of-sample validation	8 sectors including NO_x_ORM, NO_x _NRM, NO_x_SC, NO_x_OTH, VOC_ORM, VOC_IP, VOC_SU, VOC_OTH in each of the 7 regions	10 cases (Hamersley quasi-random Sequence Sampling between 0.0 and 1) for 7 regions together

[a] ORM: on-road mobile; NRM: non-road mobile; SC: stationary combustion; IP: industrial process; SU: solvent utilization; NO_x_OTH: other emission sources of NO_x (industrial process, agricultural); VOC_OTH: other emission sources of VOC (storage, non-road mobile, stationary combustion, agricultural, household).

functions established in the first step, and then the change ratio of total NO_x or VOC emissions in each source region was calculated by solving the linear functions, as expressed in equations (3) and (4).

$$E_{NOx_r} = \Delta Sectoral\_Conc_{NOx_r}/a \tag{3}$$

$$E_{VOC_r} = \Delta Sectoral\_Conc_{VOC_r}/b \tag{4}$$

where $\Delta Sectoral\_Conc_{NOx_r}$ and $\Delta Sectoral\_Conc_{VOC_r}$ are the changes in NO_x and VOC concentration respectively, in region r to local multisectoral NO_x and VOC emission changes; E_{NOx_r} and E_{VOC_r} are the ratio of total changed NO_x and VOC emissions respectively, in region r.

Lastly, the relation of NO_x or VOC emission changes to multisectoral NO_x or VOC emission changes in each source region was constructed by a series of linear functions described as equations (5) and (6), and the relative emission weight of each sector was obtained respectively. Then the change ratio of total NO_x and VOC emissions in source region under various multisectoral control scenarios can be estimated directly and participate in the calculation of the pf-ERSM system.

$$E_{NOx_r} = \sum_{j=1}^{s} w_{aj} \cdot SE_{NOx_{rj}} \tag{5}$$

$$E_{VOC_r} = \sum_{j=1}^{t} w_{bj} \cdot SE_{VOC_{rj}} \tag{6}$$

where w_{aj} and w_{bj} are the emission weight of NO_x and VOC respectively, of sector j; $SE_{NOx_{rj}}$ and $SE_{VOC_{rj}}$ are the ratio of changed NO_x and VOC emissions respectively, from sector j in region r; the superscript s and t are the number of NO_x and VOC related emission sectors, respectively.

Table 1 sums up the experiment design for constructing the pf-ERSM-SL, and Fig. S4 shows the design of the control matrix in detail. First, the O_3 response in each receptor region to NO_x and VOC emission changes in each source region (i.e., pf-RSM) was established by 42 cases of CMAQ simulations, involving in one baseline case, one zero out case and 40 control cases in which the emissions in other source regions were kept the same as the baseline. The 40 control cases were randomly sampled by Hamersley quasi-random Sequence Sampling (HSS) with a range from 0.0 to 1.5 (baseline = 1.0), and the number of 40 was recommended by previous pf-RSM research based on the number of terms in polynomial functions (Xing et al., 2018). The zero out case in the pf-RSM system was newly added compared with the traditional pf-RSM for improving the fitting accuracy near zero.

Second, the O_3 response in each receptor region to simultaneous NO_x and VOC emission changes in all source regions (i.e., pf-RSM_TT) was also created by 42 cases of CMAQ simulations, which is similar to the establishment of the single-regional pf-RSM (Xing et al., 2017; Zhao et al., 2015).

Third, on the basis of the emission inventory summarized in Table S1, NO_x and VOC emissions were divided into NO_x from on-road mobile (ORM), non-road mobile (NRM), stationary combustion (SC), and other all sectors included in the emission inventory (OTH); VOC from ORM, industrial process (IP), solvent utilization (SU), and OTH. Thus there were 8 control factors (i.e., NO_x_ORM, NO_x_NRM, NO_x_SC, NO_x_OTH, VOC_ORM, VOC_IP, VOC_SU, and VOC_OTH) involved in SL fitting for each region. Each single-regional SL system was built by one baseline case, two zero out cases in which all NO_x-related and VOC-related sectoral emissions were zeroing out, respectively, and 8 control cases in which each NO_x-related and VOC-related sectoral emission was zeroing out in turn, respectively.

Among the extra 10 cases used for out of samples (OOS) validation, sectoral NO_x and VOC emissions changed jointly in the 7 regions. In order to present a general situation, the HSS was used to sample the additional cases randomly.

2.2.2. Differential method

Sensitivity obtained by the BFM has proven to be inadaptable for retrieving the source contributions in the presence of nonlinear chemistry. As a practical method aims to quantify the source contributions, the DM divides the change ratio of NO_x and VOC emissions from single source region or sector into countless tiny intervals and sums the correspondingly tiny O_3 responses. The accumulated O_3 responses in all intervals in which only NO_x or VOC emissions changed was regarded as the contribution of NO_x or VOC emissions to O_3 response, as shown in

Table 2
The calculation process of the differential method.

Differential number	NO_x emissions [a]	VOC emissions	Response of O_3 concentration
0	$Emis_{NOx\_base}$	$Emis_{VOC\_base}$	0
1	$Emis_{NOx\_base} - d$	$Emis_{VOC\_base}$	$Cont_1\_NOx$
	$Emis_{NOx\_base} - d$	$Emis_{VOC\_base} - d$	$Cont_1\_VOC$
2	$Emis_{NOx\_base} - 2d$	$Emis_{VOC\_base} - d$	$Cont_2\_NOx$
	$Emis_{NOx\_base} - 2d$	$Emis_{VOC\_base} - 2d$	$Cont_2\_VOC$
…	…	…	…
m	$Emis_{NOx\_base} - md$	$Emis_{VOC\_base} - (m-1)d$	$Cont_m\_NOx$
	$Emis_{NOx\_base} - md$	$Emis_{VOC\_base} - md$	$Cont_m\_VOC$

[a] $d = (Emis_{NOx\_base} - Emis_{NOx\_control})/m$, due to the simultaneously changed NO_x and VOC emissions in our research, the $Emis_{VOC\_base}$ and $Emis_{VOC\_control}$ are equal to $Emis_{NOx\_base}$ and $Emis_{NOx\_control}$.

equation (7). The calculation process of the DM is given in Table 2.

$$Cont\_DM = \sum_{k=1}^{m} Cont_k\_NOx_{r\to i} + \sum_{k=1}^{m} Cont_k\_VOC_{r\to i} \quad (7)$$

where $Cont_k\_NOx_{r\to i}$ and $Cont_k\_VOC_{r\to i}$ are NO_x and VOC emission contributions respectively, from region r to O_3 response in receptor region i in the kth differential interval calculated by the DM; and m is the number of differential intervals.

The contribution of NO_x or VOC emissions from each sector to O_3 response was further apportioned by the emission weight of each sectoral NO_x or VOC estimated in the SL method, as expressed in equations (8) and (9).

$$Cont\_NOx_{r_j\to i} = \left(\sum_{k=1}^{m} Cont_k\_NOx_{r\to i}\right)\cdot\frac{w_{aj}}{\sum_{j=1}^{s} w_{aj}} \quad (8)$$

$$Cont\_VOC_{r_j\to i} = \left(\sum_{k=1}^{m} Cont_k\_VOC_{r\to i}\right)\cdot\frac{w_{bj}}{\sum_{j=1}^{t} w_{bj}} \quad (9)$$

where $Cont_NOx_{r_j\to i}$and $Cont\_VOC_{r_j\to i}$ are NO_x and VOC emission contributions respectively, from sector j in region r to O_3 response in receptor region i.

Fig. 3a shows the 2-D isopleths of O_3 response in SD to synchronous changes of NO_x and VOC emission in GZ in October 2015 (the corresponding 3-D contour is given in Fig. 3b), while NO_x and VOC emission ratios in other regions except GZ were kept unchanged. Fig. 3 is presented as a visualized example to illustrate the principle of DM and difference between the source apportionment using DM and sensitivity analysis using BFM, in which the x and y-axes reflect the ratio of VOC and NO_x emissions in GZ. As the NO_x and VOC emission ratios decrease from (1, 1) to (0, 0), which is indicated by the gray dotted line, the actual O_3 response (i.e., denoted as the impact of a synchronous emission control) is the difference between the O_3 concentration at (1, 1) and (0, 0). The accumulated O_3 responses along the blue and red paths are NO_x and VOC emission contributions respectively computed by the DM, while the O_3 responses along the blue and red dash-dot paths are the impacts of individual NO_x and VOC emission control respectively computed by the BFM. As presented in Fig. 3**d**, the sum of BFM's sensitivities is inequivalent to the actual O_3 response because of the existence of the interactions between different emission sources (Cohan et al., 2005), which limits its application in source apportionment; while the DM allocates the full individual source contribution to the actual O_3 response because its calculation process thoroughly considers the nonlinear chemistry, indicating it is an effective approach for the purpose of source apportionment. Theoretically, the more subtle the differential interval is, the closer of the changing trend of the DM to the actual change trend of O_3 concentration, according to the gray dotted line in Fig. 3a (the corresponding 3D change trend is displayed in Fig. 3b). However, what was found in our experiment was that the ratio of the contribution of VOC and NO_x kept unchanged when the number of differential intervals was greater than 118, while the computing time was continuously increasing (Fig. 3c). The ratio can be viewed as an indicator to determine the number of differential intervals, because the unchanged ratio illustrates the contribution of VOC and NO_x both remain unchanged and which further indicates that the interval is fine enough to ensure the O_3 response within each interval in linear; thus it did not make sense to differentiate further. Hence the number of differential intervals was determined as 118 eventually in the example case.

3. Results and discussion

3.1. Evaluation of the pf-ERSM-SL with differential method

Through the prediction system configured with pf-ERSM-SL, the O_3 concentrations under 10 OOS scenarios were predicted. On the basis of

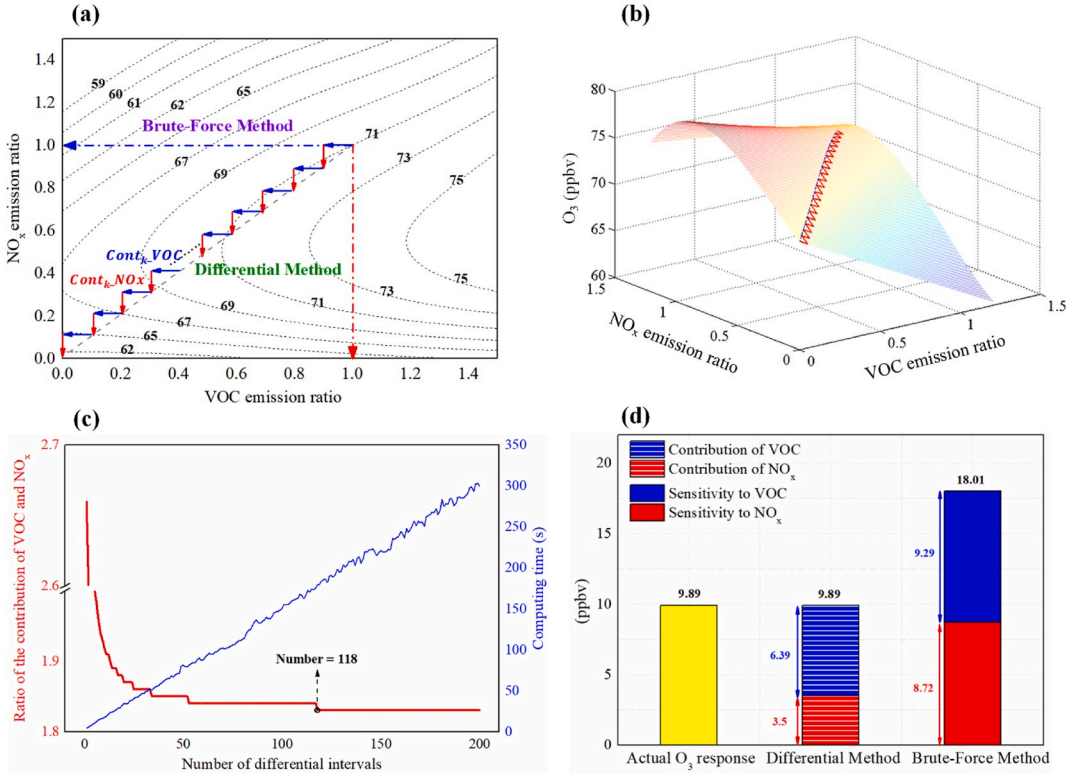

Fig. 3. (a-b) Mechanism of the DM and (c) ratio of VOC and NO_x emission contributions from GZ to O_3 response in SD and the corresponding computing time under different number of differential intervals and (d) comparison between the BFM's and DM's results. The computing time was based on the computer with a 64-bit Windows 10 system, an 8-core processor (i7-4900MQ), and a 16 GB RAM.

the indices utilized in previous researches of RSM for OOS validation, the Normalized Error (NE), Normalized Mean Error (NME), Maximum Normalized Error (MaxNE), and coefficients of correlation (R) were selected to evaluate the prediction performance of pf-ERSM-SL (**Text S2**) (Xing et al., 2011, 2017, 2018; Zhao et al., 2015, 2017). Due to the similar algorithm framework of pf-ERSM-SL and pf-RSM, the standard of the MNE within 2% and MaxNE within 10% defined in the research of pf-RSM was also applied in our study (Xing et al., 2018). Table S3 summarizes the performance of pf-ERSM-SL for predicting O_3 concentration in the whole D3 domain, and good agreement is observed in all of the 10 cases. The MNE is less than 2% in both July and October, and the relatively higher NE is found in cases with large perturbations (e.g., Case 2), which can be explained by the poor performance in edge areas with substantially controlled emissions (denoted as the marginal effects in previous RSM researches) (Xing et al., 2011, 2018). The MaxNE in July and October is 1.62% and 2.03%, respectively, and the R value is greater than 0.97 for all the 10 cases in July and October. Fig. S5 shows the statistical results of OOS validation in specific receptor region, the MNE and MaxNE in 6 regions are less than 2% and 6% in both July and October. Summarily, the statistical results across the entire D3 domain and specific receptor region both meet the defined criteria.

The pf-ERSM-SL was further applied in each grid cell of the D3 domain. Two scenarios (i.e., Case 5 and Case 9, Table S3) were selected to present two levels of emission control respectively, moderate and strict controls, to analyze the performance of the pf-ERSM-SL. It's worth noting that the performance should be similar to the two presented here despite slight variation in validation results under different control scales. Fig. 4 presents the spatial distribution of O_3 responses simulated by CMAQ and predicted by pf-ERSM-SL in two control scenarios and the corresponding delta value (i.e., pf-ERSM-SL-predicted value minus CMAQ-simulated value). In general, similar predictions are made by the pf-ERSM-SL and CMAQ for two cases, with the NE within 5% across the D3 domain in both July and October. Larger inconsistency is shown in Case 5 than in Case 9 because of the marginal effects, while the inconsistency is more evident in regions with higher O_3 concentrations because the marginal effects bring more widespread deviations in the polluted regions, as mentioned in published researches of RSM (Xing et al., 2011, 2018).

For evaluating the performance of the DM, the pf-ERSM-SL with DM was utilized to conduct the source contribution analysis when all control factors changed simultaneously. The accumulative contributions of each control factor to O_3 response calculated by the DM, the accumulative sensitivities of O_3 to abatement of individual emission source estimated by the BFM, and the actual O_3 response in each receptor region are systematically compared in Fig. S6. The accumulative contributions calculated by the DM and the actual O_3 response are the same under different control scenarios; the changing trend of the BFM's calculations is principally the same as the DM's calculations, but the accumulative sensitivities is larger than the actual O_3 response by reason of the interactions between multiple emission sources. Furthermore, several studies have mentioned that the O_3 response will more sensitive to large NO_x perturbations than that expected in the linear system, which may cause the overestimated local sensitivity under large emission reductions, especially in regions where O_3 concentrations are relatively higher (i.e., GZ in July and ZS in October) on account of the more intensive anthropogenic emissions and stronger nonlinear chemistry (Jiang et al., 2010; Wang et al., 2011b). Stronger nonlinear chemistry caused by the higher level of background O_3 and lower radical activity in the fall of the PRD may explain the larger differences between the total sensitivities and actual O_3 response in October (Li et al., 2012; Zheng et al., 2010).

The DM were then applied to estimate the accumulative contributions in the entire D3 domain when all control factors were at 100% control. By comparing the spatial distribution of the total source contributions, total sensitivities, and the actual O_3 response, the applicability of DM in the field of source apportionment was also demonstrated (Fig. 5**)**. Due to the prevailing south-westerly wind in the summer and north-easterly wind in the fall of the PRD (Li et al., 2012; Yang et al., 2019), it can be seen that the accumulative sensitivities and source contributions for downwind areas (i.e., GZ and SD in July and ZS and JM in October) are both the largest, which may be mainly influenced by the transportation of polluted plumes from the upwind areas with high NO_2 levels (Fig. S7). The magnitude of BFM's calculations across the D3 domain is still larger than the actual O_3 responses in both July and

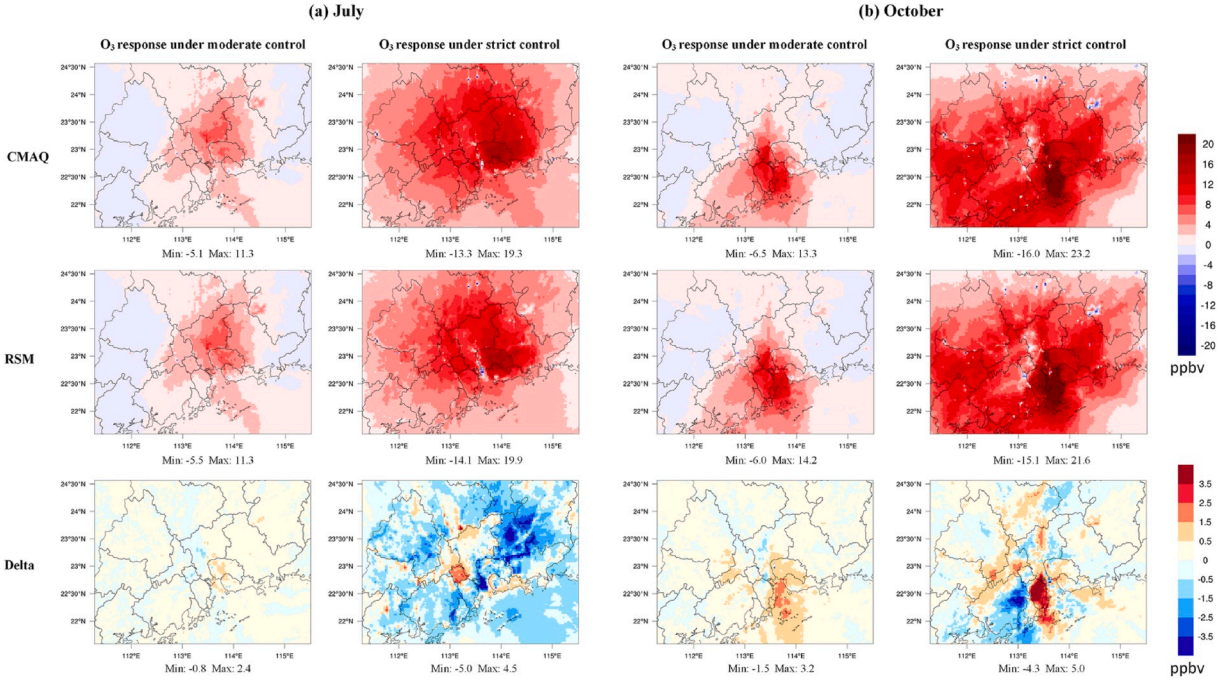

Fig. 4. Spatial distribution of the O_3 responses simulated by CMAQ and predicted by pf-ERSM-SL in two control scenarios (monthly averaged daily 1 h maxima O_3 in July and October 2015).

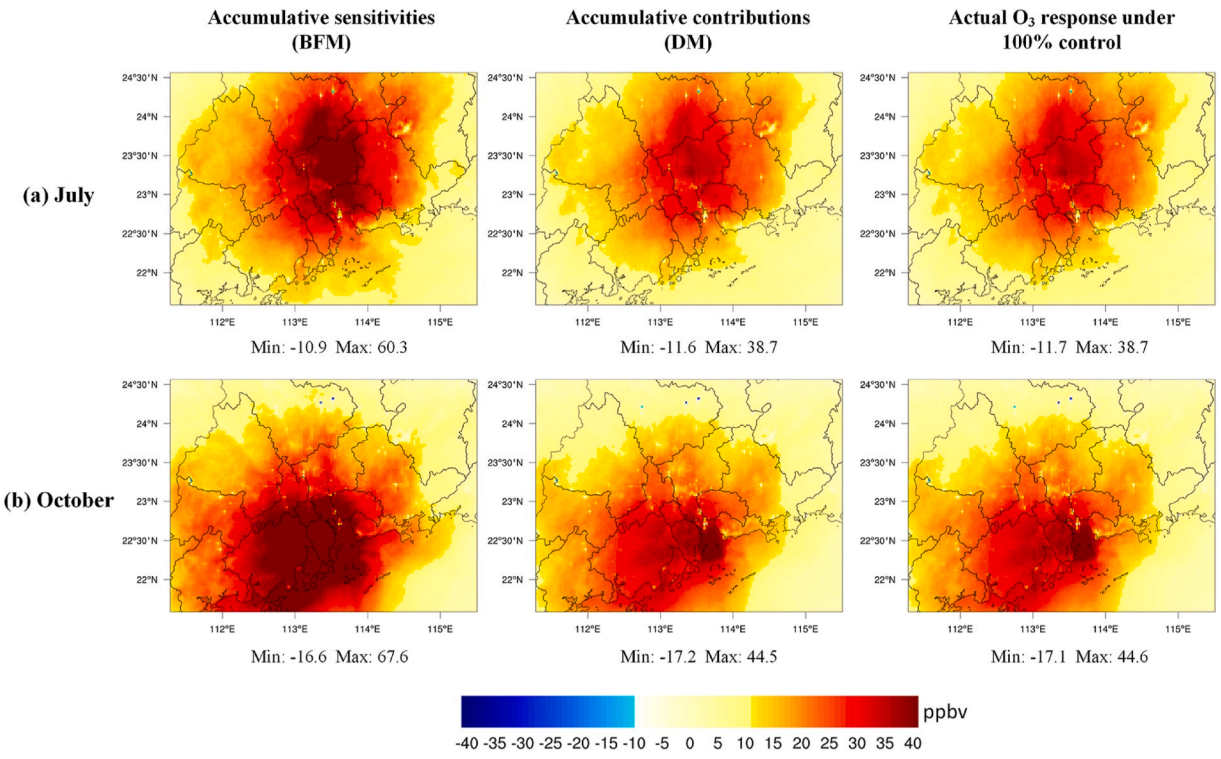

Fig. 5. Spatial distribution of the accumulative sensitivities and contributions calculated by the BFM and DM respectively, and the actual O_3 response under 100% controls of NO_x and VOC emissions in all regions (monthly averaged daily 1 h maxima O_3 in July and October 2015).

October, especially in the areas with higher O_3 concentrations. The spatial distribution of the source contributions calculated by the DM is basically the same as the actual O_3 responses in both July and October, with the discrepancies within ±0.3 ppbv and ±0.4 ppbv, respectively, in July and in October, which is mostly caused by the truncation errors. Accordingly, the DM can be regarded as an optional method for the sake of the O_3 source contribution analysis.

3.2. Identification of the O_3-NO_x-VOC relationships

Fig. 6 shows the 2-D isopleths of O_3 responses in the receptor regions to synchronous emission changes in all regions, in July and October, respectively. Defined as the NO_x emission ratio which generates maximum O_3 concentrations when VOC emissions were kept unchanged, the peak ratio (PR) for O_3 was used as an indicator determining O_3 formation regime in previous pf-RSM research (Xing et al., 2018). When a PR value below 1 (i.e., baseline), the base case is basically a VOC- limited regime, which means that the VOC reduction could effectively alleviate the O_3 level, and the NO_x reduction could make O_3 increase initially as NO titration decreases; while under other circumstance, the baseline scenario is a NO_x-limited regime; but the O_3 formation should be diagnosed as a transitional regime when the PR value is very close to 1 (i.e., 0.95–1.05). The ridgeline in the 2-D isopleths of O_3 response in October corresponds to the peak O_3 concentration produced by a given VOC emission, separating the regime limited by VOC and NO_x respectively.

For the predicted O_3 in July, the PR values are more than 1.5 in all receptor regions, even in urban areas (i.e., GZ) of the PRD, suggesting that the O_3 formations in most of the PRD regions are more sensitive to NO_x emissions in July. In October, different PR values are observed in different receptor regions but they are all lower than 1, demonstrating that the initial O_3 formation regime is both VOC-limited except that in DG&SZ, which is a transitional regime. The lower PR values at GZ (0.56), SD (0.62), and FS (0.64) are mostly caused by concentrated NO_x emissions from automobile exhausts and neighbouring coal-fired power plants. Considerable NO_x emissions from both the vehicle exhausts and agricultural vehicles and also ships may cause relatively low PR values in ZS (0.78) and JM (0.68). As for DG&SZ (0.98), abundant VOC emissions from a lot of toy, shoe, and furniture plants and workshops possibly cause the highest PR value in October. The PR values in 6 regions in July indicate that NO_x control always has a positive effect on O_3 responses in all receptor regions, even under a small reduction, while the effect of anthropogenic VOC control is small. While in October, NO_x control (with less than 22–44% reduction, $= 1 - PR$) would lead to O_3 increase in urban (i.e., GZ), industrial (i.e., SD and FS), and downwind (i.e., ZS and JM) areas of the PRD, as a result of the regime limited by VOC initially, and the O_3 formation regime would transit to NO_x-limited when NO_x emissions are further reduced.

Seasonal variation of BVOC emissions can partly explain the seasonal variation in the regime of O_3 formation (Castell et al., 2010; Chatani et al., 2015). According to past researches, BVOC emissions occupied 40% of gross VOC discharges in the summer and 22% of gross VOC discharges in fall of the PRD (Ou et al., 2015, 2016), on account of the higher temperatures and stronger sun irradiation in the summer. Figs. S8e–f shows total BVOC emissions in July and October, and it indicates that BVOC emissions in July are much higher than that in October, especially at the rural areas of JM and GZ which are covered with lush broadleaf forest, hence promoting the formation of strong NO_x-limited regime in July. As BVOC emissions descend in the fall while NO_x and AVOC emissions only change on a small scale (Figs. S8a–b), O_3 formation turns to the VOC-limited regime; besides, the VOC-limited regime may be brought by decreased radical activity caused by less ultraviolet radiation and humidity in October (Jacob et al., 1995; Wang et al., 2017b).

3.3. O_3 source contribution analysis

3.3.1. Dynamic contribution of multiregional precursor emissions to O_3

Table 3 and Fig. 7 show the contribution of specific precursor emissions from each source region to ambient O_3 concentrations in the

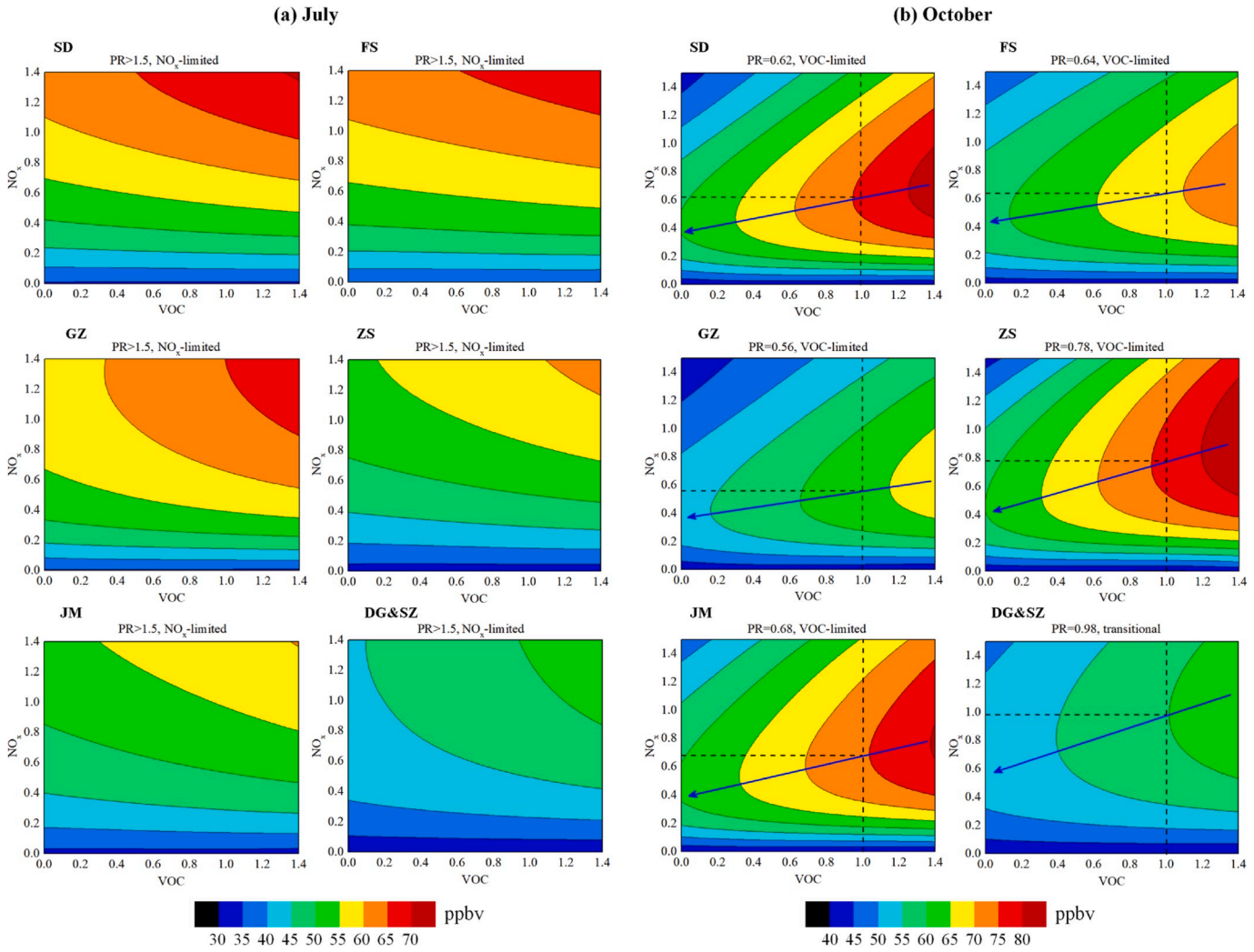

Fig. 6. 2-D isopleths of O_3 responses in the receptor regions to synchronous NO_x and VOC emission changes in all source regions (monthly averaged daily 1 h maxima O_3 in July and October 2015). The x and y-axes show the emission ratio of VOC and NO_x for the entire D3 domain; different O_3 concentrations are presented by different colors.

PRD. The real-timely dynamic source contribution analysis was conducted for monthly averaged daily 1 h maxima O_3 in July and October, and the scenarios of stepped control (i.e., reductions of 25%, 50%, 75%, and 100%) were selected.

In July, the contribution of NO_x emissions dominates in all receptor regions, while VOC emissions contribute slightly, which is consistent with the NO_x-limited regime in July. Furthermore, it can be seen that the distribution of the source contributions is analogous for different control scenarios in the receptor regions. Affected by the prevailing southwesterly wind in July, ambient O_3 concentration is comparatively higher in SD, FS, and GZ, so in these three regions, NO_x emissions from upwind areas (i.e., ZS and JM) contribute the most to O_3 formation for all control scenarios, accounting for approximately 52%, 47% and 35% of the total O_3 responses in SD, FS, and GZ respectively when at 100% control. Local NO_x emissions also have positive effects on O_3 formation in SD, FS, and GZ, with the contribution ratio ranges from 7% to 13% when at 100% control. ZS and JM are relatively in upwind areas; consequently, local NO_x emissions considerably affect the local O_3 formation, occupying about 21% and 34% of O_3 response respectively under 100% control, while NO_x emissions from OTH, which are mostly from the southern coastal areas in the D3 domain (e.g., Zhuhai), also largely influence the O_3 formation especially in ZS (~28%). As for DG&SZ, local NO_x and VOC emissions supply the most of O_3 formation for all control scenarios, while NO_x emissions from OTH is the second contributor.

In October, under 25%, 50%, and 75% controls, VOC emissions dominate O_3 formation, and NO_x emissions have different degrees of negative contribution to O_3 formation in most regions, whereas the effect of NO_x control increases evidently when at 100% control, which identifies with the regime of O_3 formation in October. Ambient O_3 concentration is comparatively higher in SD, ZS, and JM due to the prevailing north-easterly wind in October. In these three regions, VOC emissions from upwind areas (i.e., GZ and DG&SZ) are the major contributor under small perturbations (i.e., reductions of 25% and 50%), while NO_x emissions in local vehicle exhaust-intensive areas against the wind (i.e., GZ) both exhibit negative influence, especially on O_3 response in SD, which is a typical VOC-limited region. Under 75% control, VOC emissions still dominate O_3 response in SD, while in ZS and JM, the effect of NO_x control in upwind areas (i.e., GZ and DG&SZ) is emerging. When reaching 100% control, the contribution of NO_x emissions from the upwind area (i.e., GZ and DG&SZ) increases significantly for SD and ZS, accounting for about 43% and 54% of O_3 response respectively. AS for JM, NO_x emissions from each source region both partially make up the O_3 response, in which GZ contributes the most (~16%). FS, GZ, and DG&SZ are relatively in upwind areas, so local VOC emissions mainly influence O_3 formation under small perturbations (i.e., reductions of 25% and 50%), while local NO_x emissions always contribute negatively to O_3 formation in FS and GZ. As for DG&SZ, local

Table 3
O_3 source contribution in percentage by NO_x and VOC emissions from all source regions in the D3 domain under 100% control (monthly averaged daily 1 h maxima O_3 in July and October 2015).

	Receptor regions [a]	Source regions												
		NO_x						VOC						
		SD	FS	GZ	ZS	JM	DG&SZ	OTH	SD	FS	GZ	ZS	JM	DG&SZ	OTH
July	SD	7.69%	1.05%	9.56%	**25.69%**	**26.51%**	6.62%	14.70%	1.19%	0.21%	1.31%	1.17%	0.66%	3.09%	0.56%
	FS	9.82%	11.67%	8.27%	**23.84%**	**22.83%**	0.77%	17.69%	0.56%	1.95%	1.07%	0.59%	0.32%	0.32%	0.30%
	GZ	7.78%	9.37%	12.26%	**17.48%**	**17.23%**	8.99%	13.69%	0.93%	0.95%	4.83%	0.95%	0.74%	4.21%	0.59%
	ZS	0.30%	0.14%	13.35%	**20.51%**	15.23%	13.41%	**27.78%**	0.24%	0.06%	1.92%	0.86%	0.11%	4.98%	1.11%
	JM	3.34%	7.18%	6.82%	11.33%	**33.75%**	6.01%	**22.24%**	0.64%	1.15%	1.14%	1.23%	2.17%	2.55%	0.44%
	DG&SZ	0.61%	0.33%	3.02%	4.39%	8.52%	**44.03%**	**24.51%**	0.16%	0.05%	0.49%	0.73%	0.45%	11.09%	1.61%
October	SD	−3.34%	1.86%	**36.34%**	4.23%	5.35%	6.89%	4.81%	2.12%	0.42%	**18.84%**	2.27%	0.87%	16.61%	2.73%
	FS	3.26%	−1.49%	**15.52%**	6.16%	5.98%	7.45%	**31.75%**	1.91%	6.92%	9.09%	1.89%	0.75%	9.56%	1.25%
	GZ	2.10%	0.62%	−4.21%	1.54%	3.78%	16.45%	**32.32%**	1.35%	2.20%	16.18%	0.96%	1.44%	**22.18%**	3.09%
	ZS	0.95%	2.41%	**23.22%**	−1.90%	0.70%	**30.35%**	9.52%	0.28%	0.24%	7.02%	1.54%	0.13%	23.15%	2.38%
	JM	2.80%	8.35%	**15.92%**	10.67%	6.29%	12.64%	**12.98%**	4.42%	4.03%	9.08%	3.24%	2.71%	6.00%	0.87%
	DG&SZ	0.07%	0.39%	5.64%	0.15%	0.29%	**33.52%**	**35.31%**	0.31%	0.53%	2.10%	0.21%	0.21%	17.23%	4.05%

[a] SD - Shunde; FS - Foshan; GZ - Guangzhou; ZS - Zhongshan; JM - Jiangmen; DG&SZ - Dongguan&Shenzhen; OTH – other regions in the D3 domain.

VOC and NO_x emissions both positively affect the O_3 response as a result of the transitional regime in DG&SZ. Local NO_x emissions still make a negative contribution to O_3 formation in FS and GZ under 75% control, whereas the control of NO_x emissions in OTH begins to show a visible impact, which is probably due to NO_x emissions from the northern areas out of the PRD (e.g., Qingyuan). When reaching 100% control, the contribution of NO_x from upwind areas (i.e., GZ, DG&SZ, and OTH) to O_3 formation in FS and GZ increases, especially that of the NO_x from OTH, which contributes approximately 32% to O_3 response in both FS and GZ, while local NO_x emissions still present negative effect to O_3 response. As for DG&SZ, local NO_x, VOC and OTH's NO_x emission contributions to O_3 formation all nearly increase linearly with the increase in emission reductions.

3.3.2. *Contribution of multisectoral precursor emissions to O_3*

Identification of the air quality contribution of various sectoral precursor emissions is an essential prerequisite for implementing pollution control measures. In this paper, the emission inventory were divided into 8 sectors, as shown in Table 1. Source contribution results in the receptor regions regarding to these sectors are displayed in Fig. 8 for monthly averaged daily 1 h maxima O_3 in July and October.

For the source sectors inside the PRD, it can be seen that in July, NO_x_ORM emissions are the leading contributor to most of the 6 regions, with the most noticeable impact on DG&SZ (46.97%), and range from 31.68% to 42.45% on other 5 regions. NO_x_NRM emissions contribute the most to O_3 formation in JM (42.55%), while in the other 5 regions, which are the second contributor and account for 26.91%–34.91% of O_3 formation. The contribution ratio of NO_x_SC emissions ranges from 7.35% to 19.47% in the 6 regions, which is the largest in FS. The VOC-related sectoral emissions in July only make up a small part of O_3 formation in 6 regions because of the NO_x-limited regime in July. In October, NO_x_ORM and NO_x _NRM emissions still have a notable influence on O_3 formation; while VOC_ORM emissions also exhibit a considerable contribution to 6 regions, with the highest contribution to GZ (19.31%), and range from 10.58% to 16.84% to other 5 regions. Besides, VOC_SU emissions show a non-negligible effect in October, especially on O_3 formation in SD (17.26%) and GZ (16.85%).

For the sectors in each source region inside the PRD, the comprehensive analysis of source contributions in July and October was conducted. Fig. 8 suggests that GZ, DG&SZ and ZS are critical source regions of NO_x_ORM emissions to form O_3 in the receptor regions (e.g., FS in July and SD and ZS in October), as indicated in Table S1 in which GZ and DG&SZ experience the most significant NO_x_ORM emissions, resulting from intensive NO_x emissions from the vehicle exhausts in urban areas; though NO_x_ORM emissions in ZS are relatively mild, the prevailing south-westerly wind in July possibly promotes its contribution to downwind areas. The primary source regions of NO_x_NRM emissions to form O_3 are JM and OTH, as also depicted in Table S1 in which NO_x_NRM emissions are the highest in these two regions, as a consequence of intensive NO_x emissions from agricultural vehicles and ships in rural and coastal areas. GZ and ZS are major source regions of NO_x_SC emissions to form O_3, which is possibly attributed to lots of nearby coal-fired power plants in industrial areas of these two regions; while the relative higher contribution in July but moderate emissions of NO_x_SC from ZS can be also explained by the wind direction. GZ, DG&SZ and FS are regions with relatively most rapid urbanization and industrialization in the PRD, containing hundreds of industrial factories and workshops related to VOC_IP and VOC_SU emissions, and also the considerable vehicles related to VOC_ORM emissions; it can be also seen in Table S1 that GZ, DG&SZ and FS are three regions with the most advanced VOC emissions. Thus, for the sectors concerning VOC emissions, those in GZ, DG&SZ and FS display the greatest effects on O_3 formation in the receptor regions.

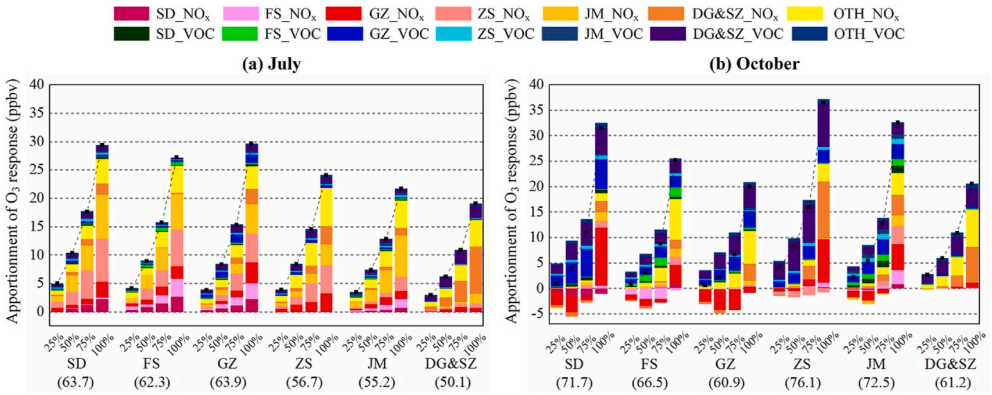

Fig. 7. Apportionment of O_3 response to the stepped controls of NO_x and VOC emissions from multiple regions (monthly averaged daily 1 h maxima O_3 in July and October 2015). The x-axis reflects the ratio of reduction (i.e., 1 – emission ratio); the number at the x-axis shows the concentration in base case; the text at the x-axis shows the receptor region; the colored bars denote the contribution of NO_x or VOC emissions from a particular region to O_3 response when all control factors are simultaneously changing; the black dotted line denotes the actual O_3 response in the scenario that all emission sources are simultaneously controlled.

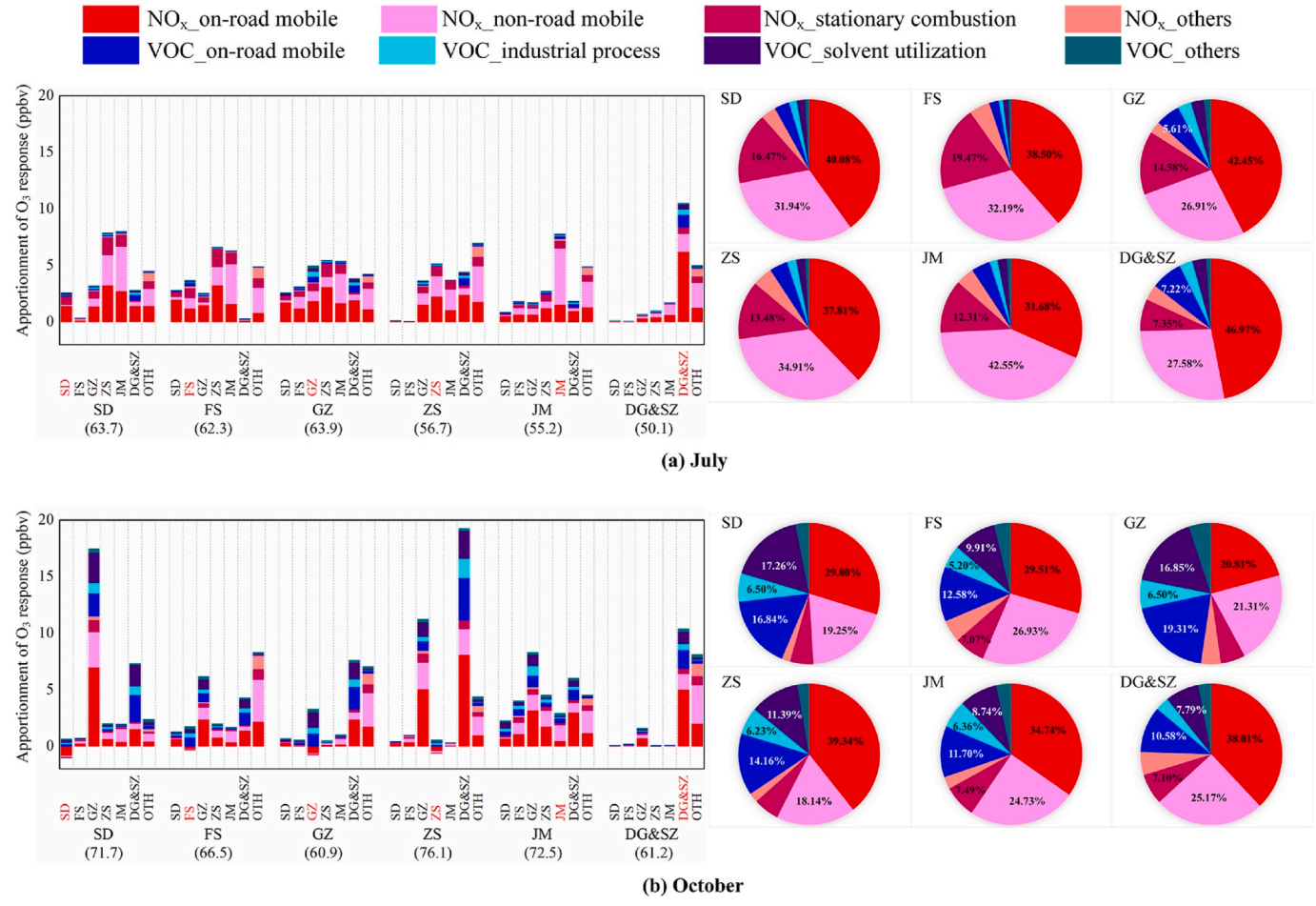

Fig. 8. Apportionment of O_3 response to the 100% controls of multisectoral NO_x and VOC emissions from each source region (left) and all source regions (right) in the D3 domain (monthly averaged daily 1 h maxima O_3 in July and October 2015). The vertical text at the x-axis reflects the source region; the horizontal text at the x-axis reflects the receptor region; the colored bars denote the contribution of NO_x or VOC emissions from a particular sector in a particular region to O_3 response when all control factors are simultaneously changing.

4. Conclusion

In this study, an enhanced meta-modeling approach, polynomial functions based ERSM coupled with the sectoral linear fitting technique (pf-ERSM-SL), combining a new differential method (DM), was developed and employed to analyze the O_3 formation regime and real-time source contributions over the PRD region. The pf-ERSM-SL had proven to show good agreement with the CMAQ simulations, and the DM was also shown to be able to effectively allocate the various source contributions to O_3, and provide the sum of individual allocations equals the actual O_3 response. Analysis of the O_3-NO_x-VOC relationships demonstrated that the O_3 formation regime in most regions of the PRD exhibited a typical NO_x-limited in July; in October, although the initial VOC-limited regime existed under small perturbations (with emissions reduction less than 22–44%), it will shift to NO_x-limited when continuing to control emissions. Further investigation of the source contributions implied that NO_x emissions from upwind areas were the most influential contributor, which largely influence the O_3 responses in

the receptor regions with higher O_3 concentrations in July and October; NO_x_ORM emissions particular these from GZ, DG&SZ and ZS were identified as the main contributor. Consequently, policymakers are advised to give priority to implement strict NO_x_ORM-focused control strategies in the PRD.

The uncertainties inherent in the meteorology and emission inventory will inevitably influence the O_3-NO_x-VOC relationships and source contribution results; hence further researches in developing the emission inventory with higher resolution are important. It is also necessary to evaluate the uncertainty of the pf-ERSM-SL with DM based on the ambient observations of NO_x and VOC, especially for VOC, which contains various species.

Declaration of competing interest

The authors declare that they have no known competing financial interests or personal relationships that could have appeared to influence the work reported in this paper.

CRediT authorship contribution statement

Tingting Fang: Conceptualization, Methodology, Software, Investigation, Writing - original draft. **Yun Zhu:** Resources, Writing - review & editing, Supervision, Project administration, Data curation. **Jicheng Jang:** Writing - review & editing, Supervision, Data curation. **Shuxiao Wang:** Resources, Writing - review & editing, Data curation. **Jia Xing:** Resources, Writing - review & editing, Data curation. **Pen-Chi Chiang:** Writing - review & editing. **Shaojia Fan:** Writing - review & editing. **Zhiqiang You:** Validation, Formal analysis, Visualization, Software. **Jinying Li:** Validation, Formal analysis, Visualization, Software.

Acknowledgments

This work was supported by the Science and Technology Program of Guangzhou, China, the National Key Research and Development Program of China (No. 2016YFC0207606), U.S. EPA Emission, Air quality, and Meteorological Modeling Support (No. EP-D-12-044), the National Natural Science Foundation of China (No. 21625701), the Fundamental Research Funds for the Central Universities (No. D2160320, D6180330, and D2170150) and the Natural Science Foundation of Guangdong Province, China (No. 2017A030310279).

Appendix A. Supplementary data

Supplementary data to this article can be found online at https://doi.org/10.1016/j.jenvman.2020.110650.

References

Burr, M.J., Zhang, Y., 2011. Source apportionment of fine particulate matter over the Eastern U.S. Part I: source sensitivity simulations using CMAQ with the Brute Force method. Atmos. Pollut. Res. 2 (3), 300–317. https://doi.org/10.5094/apr.2011.036.

Castell, N., Mantilla, E., Salvador, R., Stein, A.F., Millan, M., 2010. Photochemical model evaluation of the surface ozone impact of a power plant in a heavily industrialized area of southwestern Spain. J. Environ. Manag. 91 (3), 662–676. https://doi.org/10.1016/j.jenvman.2009.09.030.

Chatani, S., Amann, M., Goel, A., Hao, J., Klimont, Z., Kumar, A., Mishra, A., Sharma, S., Wang, S.X., Wang, Y.X., Zhao, B., 2014. Photochemical roles of rapid economic growth and potential abatement strategies on tropospheric ozone over South and East Asia in 2030. Atmos. Chem. Phys. 14 (17), 9259–9277. https://doi.org/10.5194/acp-14-9259-2014.

Chatani, S., Matsunaga, S.N., Nakatsuka, S., 2015. Estimate of biogenic VOC emissions in Japan and their effects on photochemical formation of ambient ozone and secondary organic aerosol. Atmos. Environ. 120, 38–50. https://doi.org/10.1016/j.atmosenv.2015.08.086.

Choi, K.C., Lee, J.J., Bae, C.H., Kim, C.H., Kim, S., Chang, L.S., Ban, S.J., Lee, S.J., Kim, J., Woo, J.H., 2014. Assessment of transboundary ozone contribution toward South Korea using multiple source-receptor modeling techniques. Atmos. Environ. 92, 118–129. https://doi.org/10.1016/j.atmosenv.2014.03.055.

Clappier, A., Belis, C.A., Pernigotti, D., Thunis, P., 2017. Source apportionment and sensitivity analysis: two methodologies with two different purposes. Geosci. Model Dev. (GMD) 10 (11), 4245–4256. https://doi.org/10.5194/gmd-10-4245-2017.

Cohan, D.S., Hakami, A., Hu, Y., Russell, A.G., 2005. Nonlinear response of ozone to Emissions: source apportionment and sensitivity analysis. Environ. Sci. Technol. 39 (17), 6739–6748. https://doi.org/10.1021/es048664m.

Collet, S., Kidokoro, T., Karamchandani, P., Shah, T., Jung, J., 2017. Future-year ozone prediction for the United States using updated models and inputs. J. Air Waste Manag. Assoc. 67 (8), 938–948. https://doi.org/10.1080/10962247.2017.1310149.

Dunker, A.M., 1984. The decoupled direct method for calculating sensitivity coefficients in chemical kinetics. J. Chem. Phys. 81 (5), 2385–2393. https://doi.org/10.1063/1.447938.

Dunker, A.M., Yarwood, G., Ortmann, J.P., Wilson, G.M., 2002. Comparison of source apportionment and source sensitivity of ozone in a three-dimensional air quality model. Environ. Sci. Technol. 36 (13), 2953–2964. https://doi.org/10.1021/es011418f.

Emery, C., Liu, Z., Russell, A.G., Odman, M.T., Yarwood, G., Kumar, N., 2017. Recommendations on statistics and benchmarks to assess photochemical model performance. J. Air Waste Manag. Assoc. 67 (5), 582–598. https://doi.org/10.1080/10962247.2016.1265027.

Hakami, A., Odman, M.T., Russell, A.G., 2004. Nonlinearity in atmospheric response: a direct sensitivity analysis approach. J. Geophys. Res. Atmos. 109 (D15) https://doi.org/10.1029/2003jd004502.

Han, X., Zhu, L.Y., Wang, S.L., Meng, X.Y., Zhang, M.G., Hu, J., 2018. Modeling study of impacts on surface ozone of regional transport and emissions reductions over North China Plain in summer 2015. Atmos. Chem. Phys. 18 (16), 12207–12221. https://doi.org/10.5194/acp-18-12207-2018.

Itahashi, S., Hayami, H., Uno, I., 2015. Comprehensive study of emission source contributions for tropospheric ozone formation over East Asia. J. Geophys. Res. Atmos. 120 (1), 331–358. https://doi.org/10.1002/2014jd022117.

Itahashi, S., Uno, I., Kim, S., 2013. Seasonal source contributions of tropospheric ozone over East Asia based on CMAQ-HDDM. Atmos. Environ. 70, 204–217. https://doi.org/10.1016/j.atmosenv.2013.01.026.

Jacob, D.J., Horowitz, L.W., Munger, J.W., Heikes, B.G., Dickerson, R.R., Artz, R.S., Keene, W.C., 1995. Seasonal transition from NOx- to hydrocarbon-limited conditions for ozone production over the eastern United States in September. J. Geophys. Res. 100 (D5), 9315–9324. https://doi.org/10.1029/94jd03125.

Jiang, F., Guo, H., Wang, T.J., Cheng, H.R., Wang, X.M., Simpson, I.J., Ding, A.J., Saunders, S.M., Lam, M., S, H., Blake, D.R., 2010. An ozone episode in the Pearl River Delta: field observation and model simulation. J. Geophys. Res. Atmos. 115 (22) https://doi.org/10.1029/2009JD013583.

Jin, X.M., Fiore, A.M., Murray, L.T., Valin, L.C., Lamsal, L.N., Duncan, B., Folkert Boersma, K., De Smedt, I., Abad, G.G., Chance, K., Tonnesen, G.S., 2017. Evaluating a space-based indicator of surface ozone-NOx-VOC sensitivity over midlatitude source regions and application to decadal trends. J. Geophys. Res. Atmos. 122 (19), 10231–10253. https://doi.org/10.1002/2017jd026720.

Li, J., Lu, K., Lv, W., Li, J., Zhong, L., Ou, Y., Chen, D., Huang, X., Zhang, Y., 2014. Fast increasing of surface ozone concentrations in Pearl River Delta characterized by a regional air quality monitoring network during 2006-2011. J. Environ. Sci. (China) 26 (1), 23–36. https://doi.org/10.1016/s1001-0742(13)60377-0.

Li, K., Jacob, D.J., Liao, H., Shen, L., Zhang, Q., Bates, K.H., 2019. Anthropogenic drivers of 2013-2017 trends in summer surface ozone in China. Proc. Natl. Acad. Sci. U.S.A. 116 (2), 422–427. https://doi.org/10.1073/pnas.1812168116.

Li, L., An, J.Y., Shi, Y.Y., Zhou, M., Yan, R.S., Huang, C., Wang, H.L., Lou, S.R., Wang, Q., Lu, Q., Wu, J., 2016. Source apportionment of surface ozone in the Yangtze River Delta, China in the summer of 2013. Atmos. Environ. 144, 194–207. https://doi.org/10.1016/j.atmosenv.2016.08.076.

Li, Y., Lau, A.K.H., Fung, J.C.H., Zheng, J.Y., Zhong, L.J., Louie, P.K.K., 2012. Ozone source apportionment (OSAT) to differentiate local regional and super-regional source contributions in the Pearl River Delta region, China. J. Geophys. Res. Atmos. 117 https://doi.org/10.1029/2011jd017340.

Lin, C.J., Ho, T.C., Chu, H.W., Yang, H., Chandru, S., Krishnarajanagar, N., Chiou, P., Hopper, J.R., 2005. Sensitivity analysis of ground-level ozone concentration to emission changes in two urban regions of southeast Texas. J. Environ. Manag. 75 (4), 315–323. https://doi.org/10.1016/j.jenvman.2004.09.012.

Liu, X.-H., Zhang, Y., Xing, J., Zhang, Q., Wang, K., Streets, D.G., Jang, C., Wang, W.-X., Hao, J.-M., 2010. Understanding of regional air pollution over China using CMAQ, part II. Process analysis and sensitivity of ozone and particulate matter to precursor emissions. Atmos. Environ. 44 (30), 3719–3727. https://doi.org/10.1016/j.atmosenv.2010.03.036.

Long, S.C., Zhu, Y., Jang, C., Lin, C.J., Wang, S.X., Zhao, B., Gao, J., Deng, S., Xie, J.P., Qiu, X.Z., 2016. A case study of development and application of a streamlined control and response modeling system for PM2.5 attainment assessment in China. J. Environ. Sci. 41, 69–80. https://doi.org/10.1016/j.jes.2015.05.019.

Lu, X., Hong, J., Zhang, L., Cooper, O.R., Schultz, M.G., Xu, X., Wang, T., Gao, M., Zhao, Y., Zhang, Y., 2018. Severe surface ozone pollution in China: a global perspective. Environ. Sci. Technol. Lett. 5 (8), 487–494. https://doi.org/10.1021/acs.estlett.8b00366.

Luecken, D.J., Napelenok, S.L., Strum, M., Scheffe, R., Phillips, S., 2018. Sensitivity of ambient atmospheric formaldehyde and ozone to precursor species and source types across the United States. Environ. Sci. Technol. 52 (8), 4668–4675. https://doi.org/10.1021/acs.est.7b05509.

Moghani, M., Archer, C.L., Mirzakhalili, A., 2018. The importance of transport to ozone pollution in the US Mid-Atlantic. Atmos. Environ. 191, 420–431. https://doi.org/10.1016/j.atmosenv.2018.08.005.

Nguyen, G.T.H., Shimadera, H., Uranishi, K., Matsuo, T., Kondo, A., Thepanondh, S., 2019. Numerical assessment of PM2.5 and O-3 air quality in continental Southeast Asia: baseline simulation and aerosol direct effects investigation. Atmos. Environ. 219 https://doi.org/10.1016/j.atmosenv.2019.117054.

Odman, M.T., Hu, Y.T., Russell, A.G., Hanedar, A., Boylan, J.W., Brewer, P.F., 2009. Quantifying the sources of ozone, fine particulate matter, and regional haze in the Southeastern United States. J. Environ. Manag. 90 (10), 3155–3168. https://doi.org/10.1016/j.jenvman.2009.05.028.

Ou, J., Yuan, Z., Zheng, J., Huang, Z., Shao, M., Li, Z., Huang, X., Guo, H., Louie, P.K.K., 2016. Ambient ozone control in a photochemically active region: short-term despiking or long-term attainment? Environ. Sci. Technol. 50 (11), 5720–5728. https://doi.org/10.1021/acs.est.6b00345.

Ou, J.M., Zheng, J.Y., Li, R.R., Huang, X.B., Zhong, Z.M., Zhong, L.J., Lin, H., 2015. Speciated OVOC and VOC emission inventories and their implications for reactivity-based ozone control strategy in the Pearl River Delta region, China. Sci. Total Environ. 530, 393–402. https://doi.org/10.1016/j.scitotenv.2015.05.062.

Qin, M.M., Yu, H.F., Hu, Y.T., Russell, A.G., Odman, M.T., Doty, K., Pour-Biazar, A., McNider, R.T., Knipping, E., 2019. Improving ozone simulations in the Great Lakes Region: the role of emissions, chemistry, and dry deposition. Atmos. Environ. 202, 167–179. https://doi.org/10.1016/j.atmosenv.2019.01.025.

Sharma, S., Chatani, S., Mahtta, R., Goel, A., Kumar, A., 2016. Sensitivity analysis of ground level ozone in India using WRF-CMAQ models. Atmos. Environ. 131, 29–40. https://doi.org/10.1016/j.atmosenv.2016.01.036.

Sharma, S., Sharma, P., Khare, M., 2017. Photo-chemical transport modelling of tropospheric ozone: a review. Atmos. Environ. 159, 34–54. https://doi.org/10.1016/j.atmosenv.2017.03.047.

Shen, L., Jacob, D.J., Liu, X., Huang, G.Y., Li, K., Liao, H., Wang, T., 2019. An evaluation of the ability of the Ozone Monitoring Instrument (OMI) to observe boundary layer ozone pollution across China: application to 2005-2017 ozone trends. Atmos. Chem. Phys. 19 (9), 6551–6560. https://doi.org/10.5194/acp-19-6551-2019.

Shindell, D., Kuylenstierna, J.C.I., Vignati, E., van Dingenen, R., Amann, M., Klimont, Z., Anenberg, S.C., Muller, N., Janssens-Maenhout, G., Raes, F., Schwartz, J., Faluvegi, G., Pozzoli, L., Kupiainen, K., Hoeglund-Isaksson, L., Emberson, L., Streets, D., Ramanathan, V., Hicks, K., Oanh, N.T.K., Milly, G., Williams, M., Demkine, V., Fowler, D., 2012. Simultaneously mitigating near-term climate change and improving human health and food security. Science 335 (6065), 183–189. https://doi.org/10.1126/science.1210026.

Strode, S.A., Ziemke, J.R., Oman, L.D., Lamsal, L.N., Olsen, M.A., Liu, J.H., 2019. Global changes in the diurnal cycle of surface ozone. Atmos. Environ. 199, 323–333. https://doi.org/10.1016/j.atmosenv.2018.11.028.

Tan, Z.F., Lu, K.D., Jiang, M.Q., Su, R., Dong, H.B., Zeng, L.M., Xie, S.D., Tan, Q.W., Zhang, Y.H., 2018. Exploring ozone pollution in Chengdu, southwestern China: a case study from radical chemistry to O-3-VOC-NOx sensitivity. Sci. Total Environ. 636, 775–786. https://doi.org/10.1016/j.scitotenv.2018.04.286.

Turner, M.C., Jerrett, M., Pope, C.A., Krewski, D., Gapstur, S.M., Diver, W.R., Beckerman, B.S., Marshall, J.D., Su, J., Crouse, D.L., Burnett, R.T., 2016. Long-Term ozone exposure and mortality in a large prospective study. Am. J. Respir. Crit. Care Med. 193 (10), 1134–1142. https://doi.org/10.1164/rccm.201508-1633OC.

Wang, N., Lyu, X.P., Deng, X.J., Guo, H., Deng, T., Li, Y., Yin, C.Q., Li, F., Wang, S.Q., 2016. Assessment of regional air quality resulting from emission control in the Pearl River Delta region, southern China. Sci. Total Environ. 573, 1554–1565. https://doi.org/10.1016/j.scitotenv.2016.09.013.

Wang, N., Lyu, X.P., Deng, X.J., Huang, X., Jiang, F., Ding, A.J., 2019. Aggravating O-3 pollution due to NOx emission control in eastern China. Sci. Total Environ. 677, 732–744. https://doi.org/10.1016/j.scitotenv.2019.04.388.

Wang, S.X., Xing, J., Jang, C.R., Zhu, Y., Fu, J.S., Hao, J.M., 2011a. Impact assessment of ammonia emissions on inorganic aerosols in east China using response surface modeling technique. Environ. Sci. Technol. 45 (21), 9293–9300. https://doi.org/10.1021/es2022347.

Wang, T., Xue, L.K., Brimblecombe, P., Lam, Y.F., Li, L., Zhang, L., 2017a. Ozone pollution in China: a review of concentrations, meteorological influences, chemical precursors, and effects. Sci. Total Environ. 575, 1582–1596. https://doi.org/10.1016/j.scitotenv.2016.10.081.

Wang, X.S., Zhang, Y.H., Hu, Y.T., Zhou, W., Zeng, L.M., Hu, M., Cohan, D.S., Russell, A. G., 2011b. Decoupled direct sensitivity analysis of regional ozone pollution over the Pearl River Delta during the PRIDE-PRD2004 campaign. Atmos. Environ. 45 (28), 4941–4949. https://doi.org/10.1016/j.atmosenv.2011.06.006.

Wang, Y., Wang, H., Guo, H., Lyu, X.P., Cheng, H.R., Ling, Z.H., Louie, P.K.K., Simpson, I. J., Meinardi, S., Blake, D.R., 2017b. Long-term O-3-precursor relationships in Hong Kong: field observation and model simulation. Atmos. Chem. Phys. 17 (18), 10919–10935. https://doi.org/10.5194/acp-17-10919-2017.

Xing, J., Ding, D., Wang, S.X., Zhao, B., Jang, C., Wu, W.J., Zhang, F.F., Zhu, Y., Hao, J. M., 2018. Quantification of the enhanced effectiveness of NOx control from simultaneous reductions of VOC and NH3 for reducing air pollution in the Beijing-Tianjin-Hebei region, China. Atmos. Chem. Phys. 18 (11), 7799–7814. https://doi.org/10.5194/acp-18-7799-2018.

Xing, J., Wang, S.X., Jang, C., Zhu, Y., Hao, J.M., 2011. Nonlinear response of ozone to precursor emission changes in China: a modeling study using response surface methodology. Atmos. Chem. Phys. 11 (10), 5027–5044. https://doi.org/10.5194/acp-11-5027-2011.

Xing, J., Wang, S.X., Zhao, B., Wu, W.J., Ding, D.A., Jang, C., Zhu, Y., Chang, X., Wang, J. D., Zhang, F.F., Hao, J.M., 2017. Quantifying nonlinear multiregional contributions to ozone and fine particles using an updated response surface modeling technique. Environ. Sci. Technol. 51 (20), 11788–11798. https://doi.org/10.1021/acs.est.7b01975.

Yang, W.Y., Chen, H.S., Wang, W.D., Wu, J.B., Li, J., Wang, Z.F., Zheng, J.Y., Chen, D.H., 2019. Modeling study of ozone source apportionment over the Pearl River Delta in 2015. Environ. Pollut. 253, 393–402. https://doi.org/10.1016/j.envpol.2019.06.091.

You, Z., Zhu, Y., Jang, C., Wang, S., Gao, J., Lin, C.-J., Li, M., Zhu, Z., Wei, H., Yang, W., 2017. Response surface modeling-based source contribution analysis and VOC emission control policy assessment in a typical ozone-polluted urban Shunde, China. J. Environ. Sci. 51, 294–304. https://doi.org/10.1016/j.jes.2016.05.034.

Zhang, L., Wang, T., Zhang, Q., Zheng, J.Y., Xu, Z., Lv, M.Y., 2016. Potential sources of nitrous acid (HONO) and their impacts on ozone: a WRF-Chem study in a polluted subtropical region. J. Geophys. Res. Atmos. 121 (7), 3645–3662. https://doi.org/10.1002/2015jd024468.

Zhao, B., Wang, S.X., Xing, J., Fu, K., Fu, J.S., Jang, C., Zhu, Y., Dong, X.Y., Gao, Y., Wu, W.J., Wang, J.D., Hao, J.M., 2015. Assessing the nonlinear response of fine particles to precursor emissions: development and application of an extended response surface modeling technique v1.0. Geosci. Model Dev. (GMD) 8 (1), 115–128. https://doi.org/10.5194/gmd-8-115-2015.

Zhao, B., Wu, W.J., Wang, S.X., Xing, J., Chang, X., Liou, K.N., Jiang, J.H., Gu, Y., Jang, C., Fu, J.S., Zhu, Y., Wang, J.D., Lin, Y., Hao, J.M., 2017. A modeling study of the nonlinear response of fine particles to air pollutant emissions in the Beijing-Tianjin-Hebei region. Atmos. Chem. Phys. 17 (19), 12031–12050. https://doi.org/10.5194/acp-17-12031-2017.

Zheng, J., Zhong, L., Wang, T., Louie, P.K.K., Li, Z., 2010. Ground-level ozone in the Pearl River Delta region: analysis of data from a recently established regional air quality monitoring network. Atmos. Environ. 44 (6), 814–823. https://doi.org/10.1016/j.atmosenv.2009.11.032.

Zou, Y., Charlesworth, E., Yin, C.Q., Yan, X.L., Deng, X.J., Li, F., 2019. The weekday/weekend ozone differences induced by the emissions change during summer and autumn in Guangzhou, China. Atmos. Environ. 199, 114–126. https://doi.org/10.1016/j.atmosenv.2018.11.019.